
Mathematical Simulation for Correct Coupling of Direct Solar Gain to Thermal Mass Inside a Prototypical Space

Tahar Messadi, Arch.D.

ABSTRACT

Design considerations toward the effective use of thermal mass distribution inside a space need to be supported by optimization decisions in order to adequately control the indoor thermal environment through the charging and discharging of heat. In naturally heated or cooled spaces, the thermal performance of internal mass is affected by the interior solar dynamics and the mass distribution layout within the space envelope. The placement with regard to solar exposure, the size, and the thermophysical properties are all aspects of thermal mass that must be evaluated in their contribution to the resulting profile of the inside air temperature. Among these parameters, the solar impact on the interior surfaces is the most elusive because of daily variations in solar exposure of the interior surfaces. The direct and diffuse components of solar radiation that enter a space have been commonly treated as if they were both diffuse. Such an assumption dismisses a significant aspect of the real solar impact on the space, which leads to inadequate placement of internal mass. Above all, this assumption does not comply with the understanding of solar transmission through glass.

This paper presents a more precise mathematical model of the thermal impact that each of these two radiation components has on the indoor thermal mass by considering the dynamics as a result of the sun's motion across the sky, the changing geometry and areas of the sunlit configurations cast along the room's interior surfaces, and the shifting location of these internal sunlit areas.

In addition, this paper provides a comparative analysis of the results obtained from a physical experiment and from a simulation.

INTRODUCTION

This paper presents a mathematical procedure to model the correct coupling of direct solar gain to the thermal mass distributed inside a prototypical space. Essentially, this model was developed applying modifications to the energy balance method by combining it with a method previously developed by Messadi (1990a, 1990b) regarding the precise dynamic movement of sunlit areas over the room's internal surfaces.

This new model required the adoption of two strategies. First, a mathematical model had to be formulated for the same parallelepipedic room and south-oriented rectangular window used in the algorithms yielding the dynamic sunlit areas. Second, a detailed consideration of the energy flows entering into the energy balance over each internal surface required a distinction between those areas exposed to direct solar radiation and those not so exposed. The magnitude of the solar heat absorption for specific internal sunlit areas is complicated by the changing solar exposure. One way to resolve this problem

is to subdivide each internal surface into a set of smaller equal areas. Then the thermal behavior of each sub-unit of area can be calculated as a function of time. In this way, a more accurate quantification of diffuse and direct solar intake is obtained, as well as the temperature distribution along each internal surface, as the solar configurations change in shape and location. These strategies permit the application of the heat balance control volume to each individual sub-unit area.

The mathematical modeling explicitly includes heat exchanges at the room surfaces, i.e., the convective and radiative heat transfers at the room's internal and external surfaces, heat transfer by conduction through the room's enclosure, solar load due to internal surface exposure, and heat gains or losses attributable to infiltration. The heat capacity of each component is included. The climatic variables, i.e., solar radiation, outdoor air temperature, and wind velocity, impact only the external surface of the south wall and window. Other

Tahar Messadi is an assistant professor in the College of Architecture, Georgia Institute of Technology, Atlanta.

conventional internal heat gains, such as occupancy loads, electrical lighting loads, and equipment loads, were omitted.

The heat balance method equations are from chapter 28 of *ASHRAE Fundamentals* (ASHRAE 1989) and were originally developed to calculate the instantaneous space sensible load, assuming a fixed constant indoor air temperature. But the room under study here is not conditioned and the principal interest is aimed at investigating the floating temperature fluctuations inside this space. Thus, the heat balance method was adapted to predict the floating inside surface temperatures of wall and window as well as the corresponding room air temperatures.

First, the interior surfaces are subdivided into sets of small, equal sub-units of area in order to track the solar load from the shifting sunlit areas. Essentially, a grid is superimposed over each internal surface. Hence, the gridcell unit will now define the new smaller control volume entity in terms of its lateral extent. Second, to account for the thermal impact of the room enclosure components (wall, floor, etc.), new control volumes had to be assigned to the various material layers constituting the room enclosure. The one-dimensional energy balance is applied in the thickness direction to each control volume. The thickness of the room enclosure components was discretized to suit the application of the finite difference method, implicit technique.

A further complexity arises from the radiative exchanges between the numerous gridcell units. A large number of view factors must be calculated adequately from each gridcell to all the others. Also, direct solar radiation absorption must be quantified for each gridcell.

This paper considers some specific room design considerations and general assumptions. The equations for the various nodes are discussed in detail. The paper closes with an experimental evaluation of the simulation model.

TEST CHAMBER CONSIDERATIONS AND SIMULATION ASSUMPTIONS

A mathematical simulation model is developed and is validated against experimental results obtained with a thermal test chamber, described below. The attributes of this chamber influence some of the formulation of the numerical model.

Room Design Considerations

The layout of the thermal test chamber is shown in Figure 1. The chamber is an experimental room inside a larger building with only the south wall, containing a single glazed window, exposed to outdoor conditions. The rest of the chamber is exposed to the controlled normal ambient conditions of the larger building.

The chamber, which is 6 ft wide, 8 ft long, and 6 ft, 6 in. high, is constructed of opaque enclosing panels that consist of 8 in. of beaded polystyrene sandwiched between two 7/16 in. particle boards. This insulation material has very small heat capacity so that the total thermal inertia of the test chamber is

principally related to any thermal mass added inside the chamber (Figure 1). Although practically small, the heat capacity in the opaque panels of the chamber is taken into consideration in order to reduce disagreement in the comparison between the simulated and the experimental results.

Simulation Assumptions

First, it is assumed that the heat transfer flow is one-dimensional normal to the internal surfaces. Since the lateral dimensions of the room components, i.e., a wall, are much larger than the thickness, the quantities of heat flowing laterally are considered to be negligible. Second, for simulation purposes, the temperature of the internal air is assumed to be uniform over the entire volume (as if instantaneously mixed). Third, the energy effects due to precipitation and humidity transport are not taken into account in order to better manage the scope of this investigation.

MATHEMATICAL FORMULATIONS OF ROOM TEMPERATURES

Figure 2 shows a graphic illustration of heat flows in and out of each component of the space defined by a room with one window. This figure illustrates the heat exchange by convection between the surfaces of the room components and the inside and outside air. The net heat exchange by longwave radiation between internal surfaces is also represented. Figure 2 shows the incoming direct solar radiation that strikes a localized area of the internal surface(s). A portion of that radiation is absorbed and its heat conducted through the room's internal surface(s). The reflected part is ultimately absorbed after this shortwave solar radiation bounces diffusely around the internal surfaces.

Convective Heat Transfer Coefficient

The rate of heat transfer from the surface to a wall's interior is dependent on the surface temperature, the air temperature, and air velocity along the surface as well as the conductive process through the solid material of the wall.

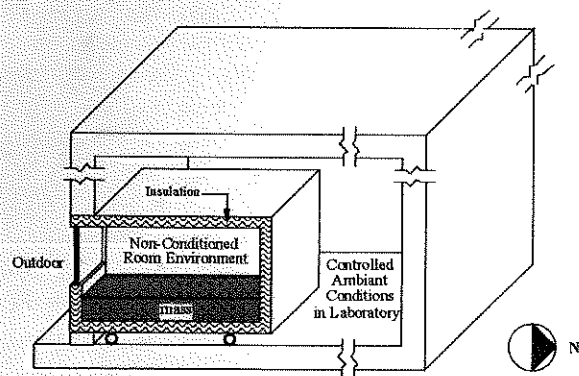


Figure 1 Room design setup.

the conduction mode of heat transfer is quantified through the application of the finite difference method, implicit technique. Once the heat balance is complete, the surface temperatures are derived for the room components.

Heat to or from Room Internal Surface: q_{si} . Again, Figure 3 displays control volumes for the internal air volume, the space-enclosing surfaces, the solid wall and glass window, and the outside surfaces. Starting with the enclosing surfaces, the ASHRAE method for heat balance begins with the heat coming into or leaving the enclosing surface. Such energy is quantified as

$$q_{si}^{p+1} = h_{ia}(T_{ia}^{p+1} - T_{si}^{p+1}) + \left(\sum_{sk=1}^n g_{(si,sk)} \cdot (T_{sk}^{p+1} - T_{si}^{p+1}) \right) + R_{si} \quad (3)$$

with

$$h_{ia}(T_{ia}^{p+1} - T_{si}^{p+1})$$

representing the heat gain by convection, and

$$\sum_{sk=1}^n g_{(si,sk)} \cdot (T_{sk}^{p+1} - T_{si}^{p+1})$$

representing the longwave radiative interchange.

R_{si} includes all other radiant energies absorbed by the surface, which consist of shortwave radiation from the window solar gains, occupants, and lights. In this study, R_{si} is considered to only represent the absorbed solar radiation penetrating through the window. The proper quantification of this parameter, R_{si} , will later be developed based on the strategies related to sunlit configurations. It is important to reiterate that these algorithms will essentially remain the same except for the adjustments imposed by the modifications brought to the control volumes due to the R_{si} parameter. As indicated before, the net heat transfer to the surfaces (both internal and external) from the air and the surroundings must be equal to the heat leaving the surface and conducted through and stored into the solid medium. The conductive and storage aspects will be presented in later sections.

Indoor Air Heat Balance: q_{ia} . Referring again to Figure 3, the heat balance for the space air volume node is developed under the assumption that the air heat capacity is not negligible. The sum of all heat flows into it must be equal to the heat stored in the air:

$$\sum_{si=1}^n A_{si} \cdot h_{si} \cdot (T_{si}^{p+1} - T_{ia}^{p+1}) + \rho_{oa} \cdot V_{oa} \cdot c_{p,oa} (T_{oa}^{p+1} - T_{ia}^{p+1}) = \rho_{ia} \cdot V_{ia} \cdot c_{p,ia} (T_{ia}^{p+1} - T_{ia}^p) \quad (4)$$

where

$$\sum_{si=1}^n A_{si} \cdot h_{si} \cdot (T_{si}^{p+1} - T_{ia}^{p+1})$$

is the convective heat from enclosing surfaces,

$$\rho_{oa} \cdot V_{oa} \cdot c_{p,oa} (T_{oa}^{p+1} - T_{ia}^{p+1})$$

is the heat loss or gain by infiltration/ventilation, and

$$\rho_{ia} \cdot V_{ia} \cdot c_{p,ia} (T_{ia}^{p+1} - T_{ia}^p)$$

is the heat intake/relief into/from the air volume.

Heat Balance at the Glass Internal Surface: q_{gi} . An equation is again used to express the net heat transfer to or from the window internal surface with respect to the heat exchange with the room air and the other room surfaces:

$$q_{gi}^{p+1} = h_{gi} \cdot A_{gi} \cdot (T_{ia}^{p+1} - T_{gi}^{p+1}) + \sum_{sk=1}^n g_{(si,sk)} \cdot A_{gi} \cdot (T_{sk}^{p+1} - T_{gi}^{p+1}) + R_{gi} \quad (5)$$

where the subscript R_{gi} represents the portion of the reflected beam radiation absorbed by the window surface and T_{gi}^{p+1} is the inside surface temperature of the glass window. In the same manner, to derive the inside surface temperature of the window, we consider that the same quantity of heat transferred, q_{gi}^{p+1} , is equivalent to the heat flowing through the window.

In order to appropriately quantify the heat flow at the inner surface of the glass, an energy balance is established. *ASHRAE Fundamentals* (ASHRAE 1989) describes the heat flow through a single DSA sheet of clear glass window, arriving at the inner glass surface by conduction and outside solar absorption and flowing into the space by convection and longwave radiation, as

$$q_{(rc,gi)}^{p+1} = U_i \cdot A_{gi} \cdot \left(\alpha_g \cdot I_o \left(\frac{1}{h_{gi}} \right) + (T_{oa}^{p+1} - T_{ia}^{p+1}) \right) \quad (6)$$

where

U_i = total window U-value, expressed in Btu/h·ft²·°F;

α_g = absorptivity value of glass, dimensionless;

I_o = outside solar radiation, expressed in Btu/h·ft²;

h_{go} = outside window surface convective heat transfer coefficient, in Btu/h·ft²·°F;

h_{gi} = inside window surface convective heat transfer coefficient, in Btu/h·ft²·°F;

T_{oa}^{p+1} = outside air temperature at time p+1, expressed in °F;

T_{ia}^{p+1} = inside air temperature at time p+1, expressed in °F.

Equation 6 is employed here to maintain consistency with the experimental setup. Obviously, in the case when there is no solar radiation, the algorithm is reduced to calculating the heat by conduction only. Therefore,

$$q_{(rc,gi)}^{p+1} = U_i \cdot A_{gi} \cdot (T_{oa}^{p+1} - T_{ia}^{p+1}) \quad (7)$$

By comparison, Equations 5 and 6 are equal, in terms of the heat removed from or coming into the glass internal surface, and are used for window energy balance:

$$h_{gi} \cdot A_{gi} \cdot (T_{ia}^{p+1} - T_{gi}^{p+1}) + \sum_{sk=1}^n s_{(gi,sk)} \cdot A_{gi} \cdot (T_{sk}^{p+1} - T_{gi}^{p+1}) = \left(U_i \cdot A_{gi} \cdot (\alpha_{gi} \cdot I \cdot \left(\frac{1}{h_{gi}} \right) + (T_{oa}^{p+1} - T_{ia}^{p+1})) \right) \quad (8)$$

Finite Difference Method (Implicit Technique)

Node Locations in Mass, Chamber Enclosure, and Their Heat Balance Equations. When mass is distributed inside, another medium is added to the room enclosure. Therefore, the heat leaving the room is first conducted through the mass, then through the room enclosure. In this situation, the finite difference method, implicit technique, is applied to calculate the heat conducted through the solid and to derive the temperature distribution within the discrete thickness of the wall. Such numerical equations give the rate of heat flowing into the mass portion and the enclosure through the conduction mode, as well as the subsequent storage of heat.

In order to use the finite difference method, the material through which heat transfers is divided up into thin elements. Each element receives heat from its adjacent element on the higher temperature side, stores some of this heat to raise its own temperature, and passes the remainder to its adjacent element on the lower temperature side.

Figure 4 shows the selected node temperature placement within their respective control volumes and indicates that the heat transfer takes place through the mass and the room envelope. While only conduction happens at the interior nodes, the surface nodes T_{si} and T_{sa} are subjected to different thermal conditions besides conduction, such as convection and radiation. In the nomenclature used, the nodes, T_{si} and T_1 to T_n are distributed over mass, while T_{f1} to T_{f6} and T_{sa} are distributed over the room frame. Notice, however, that nodes T_n and T_{f1} overlap when mass is laid over the room component and that the control volume is defined over two different types of material. For clarification, such a node will be identified as T_n when mass is distributed (Figure 4) but will be called T_{f1} when no mass is laid over the room component.

A similar situation of control volume occurs for nodes T_{f3} and T_{f5} . The same nodal nomenclature was adopted for wood and insulation components of the room frame because of the simplification it provides. To comply with the energy conservation law, a control volume is attributed to each node, and then the conservation of energy is applied to the control volume about the nodal region. Since the direction of the heat flow (into or out of the node) is often unknown, it is convenient to formulate the energy balance by assuming that all heat flows to the node (Incropera and Dewitt 1985). At this point, it becomes possible to write the complete energy balance for the interior nodes and for the internal and external surface nodes.

Mass Interior Node: T_m . The following equation will be repeated for the many defined interior nodes, T_1, T_2, \dots to T_{n-1} , distributed over a homogeneous material (Figure 4). To represent each of these discrete nodal points in the mass thickness, the following algorithm is expressed in a typical form using the subscripts $m, m+1$, and $m-1$ (Figure 4). For an internal node, the equation can be written as follows:

$$(k_m \cdot (T_{m-1}^{p+1} - T_m^{p+1}) / \Delta X_m) + (k_m \cdot (T_{m+1}^{p+1} - T_m^{p+1}) / \Delta X_m) = (\rho_m \cdot c_{p,m} \cdot \Delta X_m \cdot (T_m^{p+1} - T_m^p) / \Delta t) \quad (9)$$

where

- k_m = conduction coefficient of thermal mass, expressed in Btu/h-ft²·°F;
- ρ_m = mass density, expressed in lb/ft³;
- $c_{p,m}$ = specific heat of mass, expressed in Btu/lb·°F;
- A_m = area of mass internal surface, expressed in ft²;
- ΔX_m = discrete thickness for each thermal mass node, expressed in ft;
- Δt = time-step, h/12;
- T_{m-1}^{p+1} = temperature at node $m-1$ at future time $p+1$, expressed in °F;
- T_m^p = temperature at node m at current time p , expressed in °F;
- T_{m+1}^{p+1} = temperature at node $m+1$ at future time $p+1$, expressed in °F;
- T_m^{p+1} = temperature at node m at future time $p+1$, expressed in °F.

Through some transformations, the equation of the interior node temperature is written in the following form:

$$T_m^{p+1} = T_m^p + Fo_m \cdot (T_{m-1}^{p+1} + T_{m+1}^{p+1}) / (1 + 2Fo_m) \quad (10)$$

where the Fourier number, Fo_m , is

$$Fo_m = \alpha_{d,m} \cdot \Delta t / (\Delta X_m)^2$$

and the thermal diffusivity for mass, $\alpha_{d,m}$, is

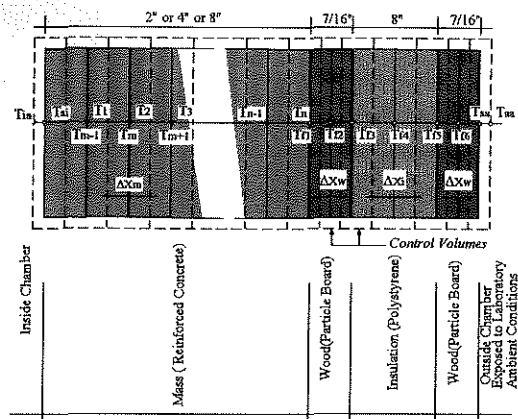


Figure 4 Location of nodal points through mass and chamber enclosure.

$$\alpha_{d,m} = k_m / (\rho_m \cdot c_{p,m}).$$

The implicit technique does not require checking for the stability criteria as does the explicit technique (Incropera and Dewitt 1985). Hence, any values can be used for the time increment, Δt , and for the discrete thickness between the nodes, ΔX . In addition, Equation 10 shows that the future temperature at node m depends on the future temperature of the adjoining nodes, $m-1$ and $m+1$.

Node located at the inside surface of mass: T_{si} . All modes of heat transfer take place at the surface node. Maintaining consistency in terms of the flow direction, the convection as well as the total radiation transfers on the left side are added to the conduction transfer on the right side as it flows into the node T_{si} :

$$q_{convection} + q_{solrad} + q_{radexch} + q_{cond} = q_{stored} \quad (11)$$

Therefore, using p as the subscript of time, the energy balance equation can be written as

$$h_{ia}(T_{ia}^{p+1} - T_{si}^{p+1}) + \left(\sum_{sk=1}^n s_{(gi,sk)} \cdot (T_{sk}^{p+1} - T_{si}^{p+1}) + R_{si} \right) + \quad (12)$$

$$k_m / \Delta X_m (T_1^{p+1} - T_{si}^{p+1}) = \rho_m \cdot c_{p,m} \cdot (\Delta X_m / 2) \cdot (T_{si}^{p+1} - T_{si}^p) / (\Delta t)$$

where T_1^{p+1} is the first discrete nodal point in the wall and T_{si}^{p+1} the inside surface temperature (see Figure 4).

Node located at the outer surface of mass: T_u . The heat balance for this node is complicated by the existence of two different mediums within the same control volume having different thermophysical properties. In addition, the contact resistance between the two surfaces is not taken into consideration. The same situation is encountered with nodes T_{f3} and T_{f5} . Thus, whenever a node is shared by two different materials, the energy balance is performed assuming that the two components are tightly sealed to one another:

$$\begin{aligned} & (k_m \cdot (T_{n-1}^{p+1} - T_n^{p+1}) / \Delta X_m) + (k_w \cdot (T_{f2}^{p+1} - T_n^{p+1}) / \Delta X_w) \\ & = (\rho_m \cdot c_{p,m} \cdot (\Delta X_m / 2) \cdot \Delta t) \\ & + (\rho_w \cdot c_{p,w} \cdot (\Delta X_w / 2) \cdot (T_n^{p+1} - T_n^p) / \Delta t) \end{aligned} \quad (13)$$

Node at the middle of the inward wood leaf: T_{f2} .

$$\begin{aligned} & (k_w \cdot (T_{f1}^{p+1} - T_{f2}^{p+1}) / \Delta X_w) + (k_w \cdot (T_{f3}^{p+1} - T_{f2}^{p+1}) / \Delta X_w) \\ & = (\rho_w \cdot c_{p,w} \cdot \Delta X_w \cdot (T_{f2}^{p+1} - T_{f2}^p) / \Delta t) \end{aligned} \quad (14)$$

Node at the outside of the inward wood leaf: T_{f3} .

$$\begin{aligned} & (k_w \cdot (T_{f2}^{p+1} - T_{f3}^{p+1}) / \Delta X_w) + (k_w \cdot (T_{f4}^{p+1} - T_{f3}^{p+1}) / \Delta X_i) = (15) \\ & (\rho_w \cdot c_{p,w} \cdot (\Delta X_w / 2) \cdot (T_{f3}^{p+1} - T_{f3}^p) / \Delta t) + (\rho_i \cdot c_{p,i} \cdot (\Delta X_i / 2) \cdot (T_{f3}^{p+1} - T_{f3}^p) / \Delta t) \end{aligned}$$

Node at the middle of the insulation thickness: T_{f4} .

$$\begin{aligned} & (k_i \cdot (T_{f3}^{p+1} - T_{f4}^{p+1}) / \Delta X_w) + (k_i \cdot (T_{f5}^{p+1} - T_{f4}^{p+1}) / \Delta X_i) \\ & = (\rho_i \cdot c_{p,i} \cdot (\Delta X_i) \cdot (T_{f4}^{p+1} - T_{f4}^p) / \Delta t) \end{aligned} \quad (16)$$

Node at outward surface of the insulation thickness: T_{f5} .

$$\begin{aligned} & (k_i \cdot (T_{f4}^{p+1} - T_{f5}^{p+1}) / \Delta X_i) + (k_w \cdot (T_{f6}^{p+1} - T_{f5}^{p+1}) / \Delta X_w) \\ & = (\rho_i \cdot c_{p,i} \cdot (\Delta X_i / 2) \cdot (T_{f5}^{p+1} - T_{f5}^p) / \Delta t) \\ & + (\rho_w \cdot c_{p,w} \cdot (\Delta X_w / 2) \cdot (T_{f5}^{p+1} - T_{f5}^p) / \Delta t) \end{aligned} \quad (17)$$

Node at the middle of the outward wood leaf: T_{f6} .

$$\begin{aligned} & (k_w \cdot (T_{f5}^{p+1} - T_{f6}^{p+1}) / \Delta X_w) + (k_w \cdot (T_{sa}^{p+1} - T_{f6}^{p+1}) / \Delta X_w) \\ & = (\rho_w \cdot c_{p,w} \cdot (\Delta X_w / 2) \cdot (T_{f6}^{p+1} - T_{f6}^p) / \Delta t) \end{aligned} \quad (18)$$

Node at outside surface of the outward wood leaf: T_{sa} .

The node T_{sa} typically represents the node at the surfaces exposed to indoor ambient conditions of the laboratory. In this case, the solar radiation is nonexistent since there is no outside exposure of these surfaces:

$$\begin{aligned} & (h_{aa} \cdot (T_{aa}^{p+1} - T_{sa}^{p+1})) + (k_w \cdot (T_{f6}^{p+1} - T_{sa}^{p+1}) / \Delta X_w) \\ & = (\rho_w \cdot c_{p,w} \cdot (\Delta X_w / 2) \cdot (T_{sa}^{p+1} - T_{sa}^p) / \Delta t) \end{aligned} \quad (19)$$

The heat balance for all nodes, including those of mass, is now complete. The next task of deriving the equation for the temperatures will be given in later sections.

Node Distribution on Test Frame Without Mass and Respective Heat Balance Equation of Each Node. When mass is not distributed at the interior surface of the chamber, the first node becomes T_{f1} as indicated above. In addition, the south wall is the component described to present the exterior surface nodal point of the wall, T_{so} , that is exposed to outdoor environmental conditions.

Node at outside surface of the outward wood leaf: T_{so} . The heat balance for node T_{so} , exposed to outdoor environmental conditions, is

$$\begin{aligned} & (\alpha_{so} \cdot I_t) + (h_{so} \cdot (T_{oa}^{p+1} - T_{so}^{p+1})) + (k_w \cdot (T_{f6}^{p+1} - T_{so}^{p+1}) / \Delta X_w) \\ & = (\rho_w \cdot c_{p,w} \cdot (\Delta X_w / 2) \cdot (T_{so}^{p+1} - T_{so}^p) / \Delta t) \end{aligned} \quad (20)$$

Node at inside surface of inward wood leaf: T_{f1} . In the no-mass situation, Figure 4 shows that the algorithms for the nodal points from T_{f2} to T_{f6} remain the same, except for node T_{f1} , which now becomes an internal surface node exposed to the air inside the chamber:

$$\begin{aligned}
 & h_{ia} \cdot (T_{ia}^{p+1} - T_{f1}^{p+1}) \\
 & + \left(\sum_{k=1}^n s_{(i,k)} \cdot (T_{sk}^{p+1} - T_{f1}^{p+1}) + (k_w \cdot (T_{f2}^{p+1} - T_{f1}^{p+1}) / \Delta X_w) \right) + R_{f1} \quad (21) \\
 & = \rho_w \cdot c_{p,w} \cdot (\Delta X_w / 2) \cdot (T_{f1}^{p+1} - T_{f1}^p) / \Delta t
 \end{aligned}$$

METHOD TO MODEL THE SOLAR RADIATION INPUT

Geometric Considerations and Purpose of Grid System

The procedure to identify the location and area of the sunlit configuration inside the room is the subject of this section. The conventional method (Kusuda 1976) considers that the directly transmitted solar radiation leaves from the inner glass surface as diffuse radiation into the indoor space. Therefore, the amount of solar heat directly received by each internal surface will only depend on the view factor between that surface and the inner glass surface. Such an assumption totally disregards the fact that the transmitted solar beam is directional and strikes defined locations on the internal surfaces.

The traditional control volume adopted for the entire area of each of the enclosing components—walls, ceiling, and floor—is no longer viable for this purpose due to the difficulties in predicting the variation in temperatures over various locations of any internal surface. The reason being that within such a control volume, it is no longer possible to distinguish between the lit and nonlit portions of any internal surface. Such an application is valid only with the assumed even distribution of solar radiation over the entire internal surface.

To track the changing sunlit areas, a grid system is superimposed over the entire internal surface of each room enclosure surface (Figure 5). Each of the surfaces of the walls, the

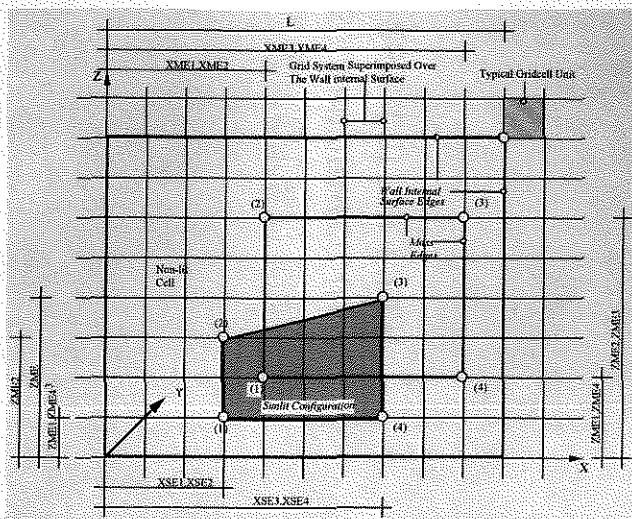


Figure 5 Typical grid layout on an internal surface of the room.

floor, and the ceiling are now divided into smaller gridcell areas defined as singular entities. The window area, however, does not need subdivision and remains an entity by itself. The gridcell units are squares of equal size. A control volume is defined over each gridcell area (Figure 5). Direct solar radiation input is counted only if a small gridcell area is at least partially lit.

The process to test which gridcells are lit and which are not can be described in the following way. At each time-step calculation, the coordinates of the sunlit configuration and the gridcell corner points are recorded. The task consists, then, of comparing the two sets of coordinates to test for overlap between the two polygons (Figure 5). The APRL (1988) Architecture Software Library contains a routine that can determine the exact superposition area between two polygons located in a three-dimensional coordinate system. The established energy balances for each room component (for instance, the west wall) can now be repeated for each gridcell of that same wall and will include the direct solar component when it strikes a gridcell.

This approach markedly increases the number of energy balances to be performed, which are a rapidly increasing function of the number of gridcells existing in the room. For instance, let us assume that $c_1, c_2, c_3, c_4, c_5,$ and c_6 are the numbers of gridcells that represent the floor, ceiling, and walls, and n_1 and n_2 represent the number of nodes chosen, respectively, through the room enclosure thickness with and without an added mass layer (Figure 5). Then the number of energy balances to be performed, except for the control volumes representing the inside air volume and the glass, can reach a maximum

$$(c_1 + c_2 + c_3 + c_4 + c_5 + c_6) \cdot n_1 \quad (22)$$

and a minimum of

$$(c_1 + c_2 + c_3 + c_4 + c_5 + c_6) \cdot n_2 \quad (23)$$

The two expressions (22 and 23) indicate that the larger the number of gridcells and the larger the number of nodes (because of more units containing mass, the larger will be the number of energy balances. In addition, through time, some of the gridcells will still happen to be partially lit as the sunlight pattern moves along the internal surface. A question is raised regarding an appropriate size for the gridcells. On one hand, smaller gridcells tend to give higher accuracy in accounting for direct solar input for the obvious reason that the presumed even distribution of solar radiation over larger, partially lit units will induce higher error in the calculated temperature. On the other hand, smaller gridcells result in a larger number of simultaneous equations, leading to more computing time and possibly the overwhelming of computer memory capacity. In addition, a large number of cumbersome view factors must be calculated to account for the radiative heat exchanges. In this situation, the manageable case is one that allows a

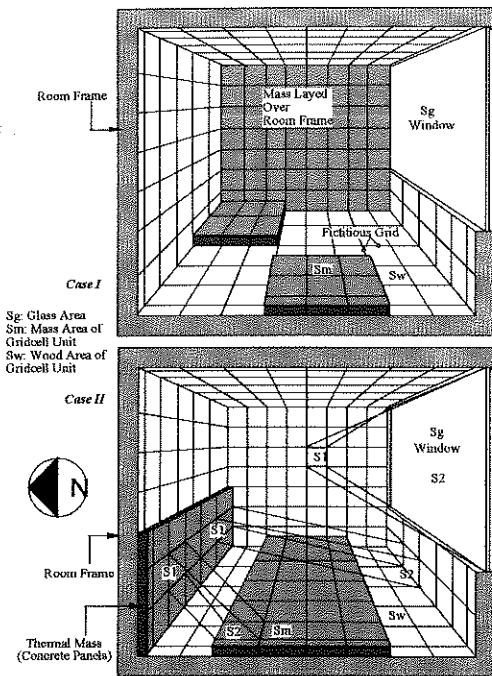


Figure 6 Ways to distribute mass over the room interior surfaces.

balanced compromise between these two imperatives with acceptable loss of accuracy.

There is also a hidden demand for computations. The energy balance gridcell computations are performed at five-minute intervals. However, due to the solar dynamics, the sunlit configurations and solar heat rates are calculated at one-minute intervals and averaged to provide the appropriate five-minute values into the gridcell computations.

Mass Distribution

Since an individual gridcell is the unit for the energy balance calculations, it offers the possibility for modeling a wide range of rather detailed mass distributions. As suggested in Figure 6, individual gridcells can either contain mass or not. Such an approach allows simulation for mass distributed anywhere inside the room.

View Factor General Formula. View factor expressions addressing two parallel surfaces of equal size and perpendicular surfaces having a common edge are available (Incropera and De Witt 1985). Such expressions are represented by $f(par)$ and $f(per)$ in Equations 24 and 25. As seen in Figure 7, various cases exist where the surfaces are not equal or have no common edge. Incropera and De Witt propose to determine the view factors for such cases by using the summation rule, but they offer no example. Hottel (1930), however, has done extensive work to combine the above two basic expressions for a more general application using the shape factor algebra. The new procedure was further clarified and simplified by Welty (1978), who reports a procedure that accommodates positioning of two surfaces—parallel or perpendicular—

within a Cartesian system, as shown in Figure 7. These surfaces may not be of equal size or have a common edge.

F_{par} is the view factor for two parallel surfaces, S_1 and S_2 (case 1 of Figure 7), and is written as:

$$\begin{aligned}
 F_{parS1-S2} = & 1/4(f(par)(x_{1,2}-x_{2,1}), (y_{1,2}-y_{2,1}), z_1) \\
 & + (f(par)(x_{1,2}-x_{2,1}), (y_{1,2}-y_{2,1}), z_1) \\
 & + (f(par)(x_{1,2}-x_{2,1}), (y_{2,2}-y_{1,1}), z_1) \\
 & + (f(par)(x_{2,2}-x_{1,1}), (y_{2,2}-y_{1,1}), z_1) \\
 & + (f(par)(x_{1,2}-x_{2,1}), (y_{1,1}-y_{2,1}), z_1) \\
 & - (f(par)(x_{1,1}-x_{2,1}), (y_{1,2}-y_{2,1}), z_1) \\
 & + (f(par)(x_{2,2}-x_{1,1}), (y_{1,1}-y_{2,1}), z_1) \\
 & - (f(par)(x_{2,2}-x_{1,2}), (y_{1,2}-y_{2,1}), z_1) \\
 & + (f(par)(x_{1,1}-x_{2,1}), (y_{2,2}-y_{1,1}), z_1) \\
 & - (f(par)(x_{2,2}-x_{1,1}), (y_{2,2}-y_{1,2}), z_1) \\
 & + (f(par)(x_{1,1}-x_{2,1}), (y_{2,2}-y_{1,1}), z_1) \\
 & - (f(par)(x_{2,2}-x_{1,1}), (y_{2,2}-y_{1,2}), z_1) \\
 & + (f(par)(x_{1,1}-x_{2,1}), (y_{1,1}-y_{2,1}), z_1) \\
 & + (f(par)(x_{2,2}-x_{1,2}), (y_{1,1}-y_{2,1}), z_1) \\
 & + (f(par)(x_{1,1}-x_{2,1}), (y_{2,2}-y_{2,1}), z_1) \\
 & + (f(par)(x_{2,2}-x_{1,2}), (y_{2,2}-y_{1,2}), z_1)
 \end{aligned} \quad (24)$$

$f(par)$ typically represents the view factor between two parallel surfaces that are of equal size and are referenced by the adjoining coordinates.

F_{per} , the general view factor formula for two perpendicular surfaces, S_1 and S_2 (case 2 of figure 7), is written as:

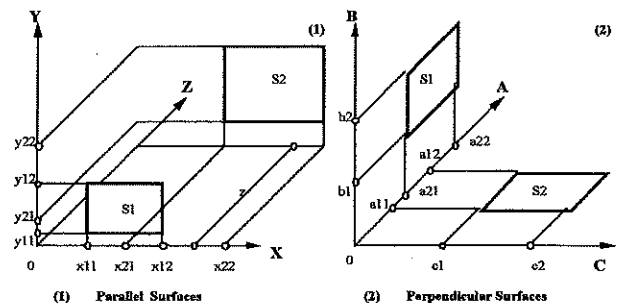


Figure 7 General view configuration between two surfaces.

$$\begin{aligned}
F_{perS1-S2} = & 1/2(f(per)(a_{2,1}-a_{1,2}), (b_2-b_0), (c_2-c_0)) \\
& -f(per)(a_{2,1}-a_{1,2}), (b_2-b_0), (c_1-c_0) \\
& +f(per)(a_{2,2}-a_{1,1}), (b_2-b_0), (c_2-c_0) \\
& -f(per)(a_{2,2}-a_{1,1}), (b_2-b_0), (c_1-c_0) \\
& +f(per)(a_{2,1}-a_{1,2}), (b_1-b_0), (c_2-c_0) \\
& +f(per)(a_{2,1}-a_{1,2}), (b_1-b_0), (c_1-c_0) \\
& -f(per)(a_{2,2}-a_{1,1}), (b_1-b_0), (c_2-c_0) \\
& +f(per)(a_{2,2}-a_{1,1}), (b_1-b_0), (c_1-c_0) \\
& -f(per)(a_{2,1}-a_{1,1}), (b_2-b_0), (c_2-c_0) \\
& +f(per)(a_{2,1}-a_{1,1}), (b_2-b_0), (c_1-c_0) \\
& -f(per)(a_{2,2}-a_{1,2}), (b_2-b_0), (c_2-c_0) \\
& +f(per)(a_{2,2}-a_{1,2}), (b_2-b_0), (c_1-c_0) \\
& +f(per)(a_{2,1}-a_{1,1}), (b_1-b_0), (c_2-c_0) \\
& -f(per)(a_{2,1}-a_{1,1}), (b_1-b_0), (c_1-c_0) \\
& +f(per)(a_{2,2}-a_{1,2}), (b_1-b_0), (c_2-c_0) \\
& -f(per)(a_{2,2}-a_{1,2}), (b_1-b_0), (c_1-c_0) \quad (25)
\end{aligned}$$

$f(per)$ typically represents the view factor between two perpendicular surfaces that have one common edge and are referenced by the adjoined coordinates.

Internal Distribution of Solar Radiation Penetrating Through the Window

The solar heat absorbed by each gridcell was identified as R_{si} or R_{gi} in the previous heat balance equations. It is appropriate, at this point, to give a full explanation of all aspects relevant to the determination of these factors and produce the corresponding algorithms.

Determination of Incoming Beam Radiation, (qb), Absorbed by Internal Gridcells. The internal surface of interest is now the surface of a gridcell, and all of the following algorithms apply to it. At first, the proper quantification of the direct beam radiation entering each gridcell surface is addressed. Then a separate approach is presented for the incoming diffuse radiation. In considering the radiant heat taken up by any internal surface, Clark (1987) presented the following form:

$$q_{dir,i} = q_{abs,i} + q_{absorbed\ of\ rays\ reflected\ from\ other\ surfaces} \quad (26)$$

where

$q_{dir,i}$ = the combined absorbed heat from the solar beam coming directly into gridcell unit i and reflected from other gridcell units $j = 2$ to n and

$q_{i,absorbed}$ = solar energy directly absorbed by surface (gridcell) i .

A proper analysis must include the effects of multiple reflections. To simplify the analysis, the reflected portion of the direct beam is assumed diffuse and apportioned onto other surfaces on the basis of view factors.

Beginning with the quantity of direct beam radiation penetrating through the window,

$$qb_{dir} = qb_{out} \cdot \tau_g \cdot A_g \quad (27)$$

where

qb_{dir} = beam solar radiation transmitted through the window, expressed in Btu/h·ft²;

qb_{out} = outside beam radiation, expressed in Btu/h·ft² (for the experimental work, qb_{out} is directly measured);

A_g = window aperture, expressed in ft²;

τ_g = transmissivity coefficient, dimensionless.

The transmissivity coefficient, τ_g , for direct beam radiation is expressed in the *DOE-2 Engineers Manual* (LBL 1982) as a polynomial in the cosine of the incident angle, $\cos \theta$, onto the window glass:

$$\tau_g = X1 + (X2 \cdot \cos \theta) + (X3 \cdot (\cos \theta)^2) + (X4 \cdot (\cos \theta)^3) \quad (28)$$

The values of $X1$, $X2$, $X3$, and $X4$ depend on the window glass type and the number of panes. Representative values are listed in the DOE-2 manual. In the absence of direct beam radiation striking the glass, τ_g is equated to 0.

Considering the directional nature of the beam radiation, the first amount of energy flux absorbed over the sunlit area is

$$qb_{abs} = qb_{dir} \cdot \alpha \quad (29)$$

where

qb_{abs} = absorbed portion of incoming beam radiation, expressed in Btu/h·ft², and

α = absorptivity of the internal surface room component, dimensionless.

Therefore, knowing which gridcells are sunlit, it becomes possible to determine the flux absorbed into the surface of each of them. Likewise, the reflected flux is

$$qb_{ref} = qb_{dir} \cdot \rho \quad (30)$$

where

qb_{ref} = reflected portion after first impact of outside incoming beam radiation, expressed in Btu/h·ft², and

ρ = reflectivity of the internal surface room component, dimensionless.

Given that the absorptivity and the reflectivity coefficients for an opaque material add up to unit, the reflectivity coefficient can be expressed by

$$\rho = 1 - \alpha \quad (31)$$

Therefore, substituting ρ in equation 30 gives

$$qb_{ref} = qb_{dir} \cdot (1 - \alpha) \quad (32)$$

Clark (1987) also suggests that an expression obtained from the ratio of Equations 29 and 32 can be useful:

$$qb_{ref}/qb_{abs} = (qb_{dir} \cdot (1 - \alpha))/(qb_{dir} \cdot \alpha) \quad (33)$$

which leads to

$$qb_{ref} = qb_{abs} \cdot (1 - \alpha)/\alpha \quad (34)$$

The reflected flux is then assumed to be diffuse and is distributed on the other gridcells according to the shape factor information. The amount of flux gridcell i receives by reflection from another gridcell, j , is written as

$$qb_{abs,i} = qb_{ref,j} \cdot F_{ji} \quad (35)$$

or as

$$qb_{abs,i} = ((qb_{dir,j} \cdot (1 - \alpha_j))/(\alpha_j)) \cdot F_{ji} \quad (36)$$

An expression can now be written for the total flux absorbed at a gridcell due to the direct solar beam entering the room; included are the direct component incident on gridcell i plus an accumulation of all of the direct beam flux, which is diffusely reflected about the room to ultimately become absorbed on gridcell i :

$$qb_{abs,i,tot} = (qb_{dir,i,b} \cdot \alpha_i) + \sum_{j=1}^n (qb_{j,ref,tot} \cdot F_{ji}) \quad (37)$$

Replacing $q_{j,ref,tot}$ by its equivalent in Equation 36 will give

$$qb_{abs,i,tot} = (qb_{dir,i,b} \cdot \alpha_i) + \sum_{j=1}^n (qb_{j,ref,tot} \cdot (1 - \alpha_j)/\alpha_j \cdot F_{ji}) \quad (38)$$

Thus, Equation 38 expresses the total absorbed heat flux from direct radiation entering through the window. Therefore, Equation 38 is repeated for every gridcell to obtain a set of n simultaneous equations that account for all of the direct flux. Obviously, for those gridcells that are not sunlit, the direct component will vanish but not the reflected accumulation. For more clarity, Equation 38 is rewritten below for gridcells 1, 2, and n (n represents the total number of grid units in the room).

The equation for gridcell 1 is

$$\begin{aligned} qb_{abs,1,tot} = & ((qb_{dir,1} \cdot \alpha_1) + (qb_{abs,1,tot}(1 - \alpha_1))/\alpha_1) \cdot F_{11} \\ & + ((qb_{abs,2,tot}(1 - \alpha_2))/\alpha_2) \cdot F_{21} + (qb_{abs,3,tot}(1 - \alpha_3))/\alpha_3) \cdot F_{31} \\ & + (qb_{abs,4,tot}(1 - \alpha_4))/\alpha_4) \cdot F_{41} + \dots + \dots \\ & + (qb_{abs,n,tot}(1 - \alpha_n))/\alpha_n) \cdot F_{n1} \end{aligned} \quad (39)$$

The equation for gridcell unit 2 is

$$\begin{aligned} qb_{abs,2,tot} = & ((qb_{dir,2} \cdot \alpha_1) + (qb_{abs,1,tot}(1 - \alpha_1))/\alpha_1) \cdot F_{12} \\ & + ((qb_{abs,2,tot}(1 - \alpha_2))/\alpha_2) \cdot F_{22} + (qb_{abs,3,tot}(1 - \alpha_3))/\alpha_3) \cdot F_{32} \\ & + (qb_{abs,4,tot}(1 - \alpha_4))/\alpha_4) \cdot F_{42} + \dots + \dots \\ & + (qb_{abs,n,tot}(1 - \alpha_n))/\alpha_n) \cdot F_{n2} \end{aligned} \quad (40)$$

And the n^{th} equation form for the n^{th} unit is

$$\begin{aligned} qb_{abs,n,tot} = & ((qb_{dir,2} \cdot \alpha_2) + (qb_{abs,1,tot}(1 - \alpha_1))/\alpha_1) \cdot F_{1n} \\ & + ((qb_{abs,2,tot}(1 - \alpha_2))/\alpha_2) \cdot F_{2n} + (qb_{abs,3,tot}(1 - \alpha_3))/\alpha_3) \cdot F_{3n} \\ & + (qb_{abs,4,tot}(1 - \alpha_4))/\alpha_4) \cdot F_{4n} + \dots + \dots \\ & + (qb_{abs,n,tot}(1 - \alpha_n))/\alpha_n) \cdot F_{nn} \end{aligned} \quad (41)$$

The view factor F_{ij} vanishes for $i=j$ since a gridcell cannot see itself ($F_{11}, F_{22}, \dots, F_{nn}=0$).

Determination of Absorbed Incoming Diffuse Radiation: qd . The diffuse radiation entering through the window glass area is directly apportioned over each gridcell unit using the view factor between the glass area and the other gridcell units. Starting with the diffuse energy transmitted through glass,

$$qd_{tr} = qd_{out} \cdot \tau_g \quad (42)$$

Assuming that all transmitted diffuse energy is internally absorbed, then

$$qd_{abs,i,tot} = qd_{tr} \cdot F_{gi} \quad (43)$$

where

$qd_{abs,i,tot}$ = absorbed energy from entering diffuse solar radiation by gridcell i , and

F_{gi} = view factor between the glass surface, g , and gridcell unit i .

In summary, the parameter R_i , which represents the total solar radiation entering the gridcell or glass internal surface, is

$$R_i = qb_{abs,i,tot} + qd_{abs,i,tot} \quad (44)$$

Considering the whole simulation problem, first, the set of equations for the view factors needs to be solved. Next, the identification of the various gridcells receiving direct solar radiation is carried out via geometric information for the sunlit configurations. Then, at each time-step, the equations to determine the heat flux R_i absorbed by each gridcell or the window glass are simultaneously solved using matrix algebra. Finally, the results are incorporated as input values for R_i and F_{ij} into the general algorithms for the determination of the node temperatures. These temperature algorithms constitute another set of equations to be solved simultaneously. The derived temperatures are published below.

Summary of All Derived Temperatures

At this point, a summary of all the temperature equations is displayed for all nodes. The parameter R_p , representing all internal heat sources, has been presented above but will not be expanded into the following algorithms. In addition, the area parameter will also be omitted.

Indoor air heat balance

$$T_{ia}^{p+1} = \sum_{si=1}^n h_{si} \cdot (T_{si}^{p+1}) + \rho_{oa} \cdot V_{oa} \cdot c_{p,oa} (T_{oa}^{p+1}) + \rho_{ia} \cdot V_{ia} \cdot c_{p,ia} (T_{ia}^{p+1}) / (\rho_{ia} \cdot V_{ia} \cdot c_{p,ia}) + \left(\sum_{si=1}^n h_{si} \right) + (\rho_{oa} \cdot V_{oa} \cdot c_{p,oa}) \quad (45)$$

Window internal surface heat balance

$$T_{gi}^{p+1} = h_{gi} (T_{ia}^{p+1}) + \left(\sum_{sk=1}^n g_{(gi,sk)} \cdot (T_{sk}^{p+1}) + R_{gi} - U_i (\alpha_g I_i (1/h_{gi})) + (T_{oa}^{p+1} - T_a^{p+1}) \right) / \left(h_{gi} \cdot \sum_{sk=1}^n g_{(gi,sk)} \right) \quad (46)$$

Mass interior node

$$T_m^{p+1} = T_m^p + Fo_m \cdot (T_{m-1}^{p+1} - T_{m+1}^{p+1}) / (1 + 2Fo_m) \quad (47)$$

with

$$Fo_m = k_m \cdot \Delta t / (\rho_m \cdot c_{p,m} \cdot \Delta X_m^2)$$

Exterior node located at the inside surface of mass

$$T_{si}^{p+1} = h_{ia} \cdot (T_{ia}^{p+1}) + \sum_{sk=1}^n (g_{(gi,sk)} \cdot (T_{sk}^{p+1}) + R_i) + (k_m / \Delta X_m) \cdot T_1^{p+1} / (\rho_m \cdot c_{p,m} \cdot (\Delta X_m / 2\Delta t)) + h_{ia} + \left(\sum_{k=1}^n (g_{i,k}) \right) + (k_m / \Delta X_m) \quad (48)$$

Node located at the outer surface of mass: T_n

$$T_n^{p+1} = (k_m \cdot T_{m-1}^{p+1} / \Delta X_m) + (k_w \cdot T_{f2}^{p+1} / \Delta X_w) + (\rho_m \cdot c_{p,m} \cdot (\Delta X_m / 2\Delta t)) + (\rho_w \cdot c_{p,w} \cdot (\Delta X_w / 2\Delta t)) (T_n^p) / ((k_m / \Delta X_m) + (k_w / \Delta X_w)) + (\rho_m \cdot c_{p,m} \cdot (\Delta X_m / 2\Delta t)) + (\rho_w \cdot c_{p,w} \cdot (\Delta X_w / 2\Delta t)) \quad (49)$$

Node at the middle of the inward wood skin of the wall sandwich panel: T_{f2}

$$T_{f2}^{p+1} = T_{f2}^p + (Fo_w \cdot (T_{f1}^{p+1} - T_{f3}^{p+1})) / (1 + 2Fo_w) \quad (50)$$

with

$$Fo_w = k_w \cdot \Delta t / (\rho_w \cdot c_{p,w} \cdot \Delta X_w^2)$$

Node at the outside of the inward wood skin of the wall sandwich panel: T_{f3}

$$T_{f3}^{p+1} = (k_w \cdot T_{f2}^{p+1} / \Delta X_w) + (k_i \cdot T_{f4}^{p+1} / \Delta X_i) + (\rho_w \cdot c_{p,w} \cdot (\Delta X_w / 2\Delta t)) + (\rho_i \cdot c_{p,i} \cdot (\Delta X_i / 2\Delta t)) (T_{f3}^p) / ((k_w / \Delta X_w) + (k_i / \Delta X_i)) + (\rho_w \cdot c_{p,w} \cdot (\Delta X_w / 2\Delta t)) + (\rho_i \cdot c_{p,i} \cdot (\Delta X_i / 2\Delta t)) \quad (51)$$

Node at the middle of the insulation thickness: T_{f4}

$$T_{f4}^{p+1} = T_{f4}^p + (Fo_i \cdot (T_{f3}^{p+1} - T_{f5}^{p+1})) / (1 + 2Fo_i) \quad (52)$$

with

$$Fo_i = k_i \cdot \Delta t / (\rho_i \cdot c_{p,i} \cdot \Delta X_i^2), \text{ then:}$$

Node at the outward of the insulation thickness: T_{f5}

$$T_{f5}^{p+1} = (k_i \cdot T_{f4}^{p+1} / \Delta X_i) + (k_w \cdot T_{f6}^{p+1} / \Delta X_w) + (\rho_i \cdot c_{p,i} \cdot (\Delta X_i / 2\Delta t)) + (\rho_w \cdot c_{p,w} \cdot (\Delta X_w / 2\Delta t)) (T_{f5}^p) / ((k_i / \Delta X_i) + (k_w / \Delta X_w)) + (\rho_i \cdot c_{p,i} \cdot (\Delta X_i / 2\Delta t)) + (\rho_w \cdot c_{p,w} \cdot (\Delta X_w / 2\Delta t)) \quad (53)$$

Node at the middle of the outward wood skin of the wall sandwich panel: T_{f6}

$$T_{f6}^{p+1} = T_{f6}^p + (Fo_w \cdot (T_{f5}^{p+1} - T_{sa}^{p+1})) / (1 + 2Fo_w) \quad (54)$$

with

$$Fo_w = k_w \cdot \Delta t / (\rho_w \cdot c_{p,w} \cdot \Delta X_w^2), \text{ then:}$$

Node at outside surface of outward wood skin of the wall sandwich panel: T_{sa}

The node T_{sa} represents the surfaces exposed to indoor ambient conditions of the laboratory. In this case, the solar radiation is nonexistent since there is no outside exposure of these surfaces:

$$T_n^{p+1} = (h_{aa} \cdot T_{aa}^{p+1}) + (k_w \cdot T_{f6}^{p+1} / \Delta X_w) + ((\rho_w \cdot c_{p,w} \cdot \Delta X_w \cdot T_{sa}^p) / 2\Delta t) / (h_{aa} + (k_w / \Delta X_w) + (\rho_w \cdot c_{p,w} \cdot (\Delta X_w / 2\Delta t))) \quad (55)$$

Node at outside surface of outward wood skin of the wall sandwich panel: T_{so}

$$T_{so}^{p+1} = (\alpha_{so} \cdot I_p) + (h_{so} \cdot T_{oa}^{p+1}) + (k_w \cdot (T_{f6}^{p+1} / \Delta X_w)) + (\rho_w \cdot c_{p,w} \cdot (\Delta X_w / 2) \cdot T_{so}^p) / (h_{so} + (k_w / \Delta X_w) + (\rho_w \cdot c_{p,w} \cdot (\Delta X_w / 2 \Delta t))) \quad (56)$$

Node at inside surface of inward wood skin of the wall sandwich panel: T_{f1}

$$T_{f1}^{p+1} = h_{ia} \cdot (T_{ia}^{p+1}) + \left(\sum_{sk=1}^n g_{(i,k)} \cdot (T_{sk}^{p+1}) + (k_w / \Delta X_w) \cdot T_{f2}^{p+1} \right) / (R_i) + \rho_w \cdot c_{p,w} \cdot (\Delta X_w / 2 \Delta t) \cdot (T_{f1})^p / h_{ia} + \left(\sum_{sk=1}^n g_{(i,k)} \right) + (k_w / \Delta X_w) + (\rho_w \cdot c_{p,w} \cdot (\Delta X_w / 2 \Delta t)) \quad (57)$$

COMPARISON BETWEEN SIMULATED AND EXPERIMENTAL RESULTS

The focus of this section is to compare the results generated from the computer simulation and the validation experiment. The resulting average indoor air temperature and the measured internal surface temperature of mass and room enclosure are the principal indicators sought in this experiment and, as such, are compared to those derived from the simulation. A first test was specifically designed to monitor the performance of the base model, i. e., without the addition of mass. In the second experiment, mass that consists of 2 in. thick concrete panels is distributed over the total area of the floor (Figure 8). In this paper, the results from both the experimental work and the simulation are discussed for the second

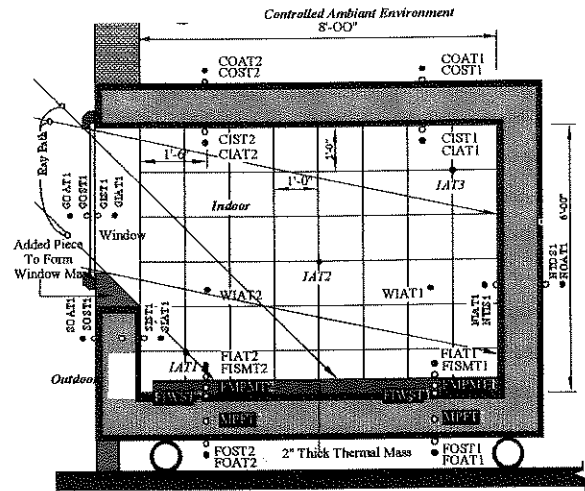


Figure 8 Section through the thermal test chamber showing thermocouple locations and thermal mass.

experiment only. First, the comparative analysis between the measured and the predicted temperatures is shown for the indoor air. Second, predicted vs. measured temperature nodes are compared, respectively, for the floor and the east wall interior surfaces.

Comparison Between Predicted and Experimental Indoor Air Temperatures

Figure 9 shows the plots of the three measured and the predicted indoor air temperatures, as well as plots of the outdoor air temperature and the solar radiation represented by

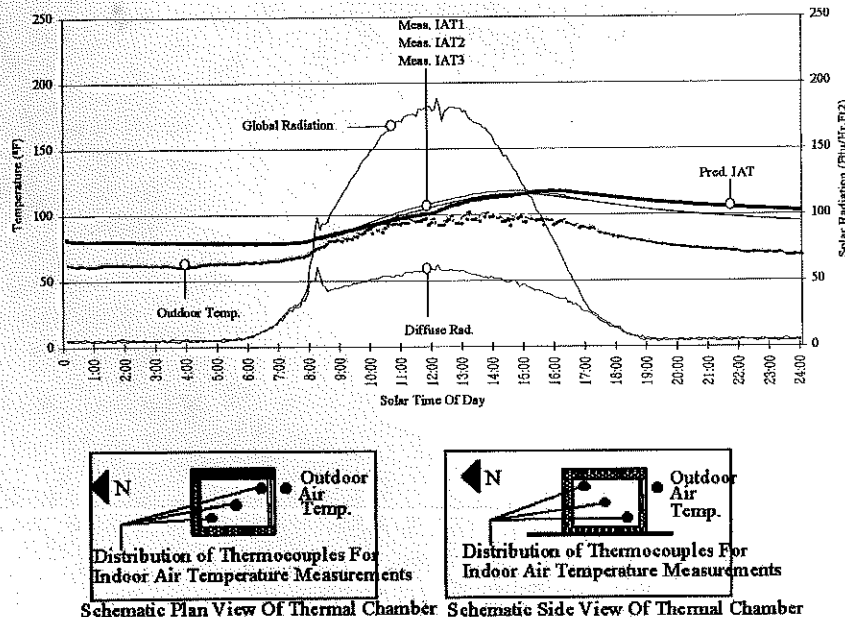


Figure 9 Comparison between measured vs. predicted indoor air temperature recorded in base case model (with mass layout).

TABLE 1
Statistical Regression Between Measured and Predicted Indoor Air Temperature

Regression: V=IAT2, PRED.IAT Cases=All Least Squares Regression						
Analysis of Variance of 4.MEAS.IAT2 N= 288 out of 288						
0	Source	DF	Sum Sqrs.	Mean Sqr.	F-Stat	SIGNIF
0	Regression	1	50415	50415	4719.8	0
9	Error	286	3055.0	10.682		
9	Total	287	53470			
0	MULT R= .97101	R-SQR= .94287	SE= 3.2683			
0	Variable	Partial	Coeff.	Std. Error	T-Stat.	Signif.
0	Constant		6.8986	1.2932	5.3346	0.0000
6	PRED.IAT	.97101	.91070	.13256 -1	68.700	0

its global and diffuse components. The deviation of the predicted indoor air temperature (Pred.IAT) from the measured ones is a little more pronounced during nighttime. The diurnal curves of the predicted and measured temperatures are in close agreement in amplitude, which varies between 77°F and 119°F. However, the plot of the predicted temperature is slightly shifted to the right, i.e., apparently slightly more time lag. The disagreement is especially evident during early morning and nighttime (Figure 9). Probably the thermophysical values assigned to the added mass are slightly high compared to those of the experiment.

Table 1 shows the statistical analysis performed between one measured indoor air temperature, IAT2, and the predicted indoor air temperature, PRED.IAT. A resulting R^2 equal to 0.94287 indicates close overall agreement.

COMPARISON BETWEEN PREDICTED VS. MEASURED

Temperatures at Selected Gridcells of Inside Surfaces

Figures 10 and 11 show comparisons between the predicted and the experimental temperatures on some of the interior surfaces of the chamber when mass is included on the floor. Again, the predicted temperature starts to rise sooner than the measured one but with smaller deviation. Node (7,4) of the floor shown in Figure 10 b and node (7,3) in Figure 11b are good examples, illustrating this early rise in the predicted temperature, although similar temperature deviations can be consistently observed in Figures 10 and 11. In Figure 10(b) the predicted temperature of node (7,4) begins the steeper rise at 8:45 a.m. while the measured one starts rising at 9:30 a.m. However, as time runs on, the predicted temperature rise slows for node (7,4) to attain a maximum of 124°F, 10°F lower than

the maximum temperature found by experiment. The same argument could be made about the thermal inertia in the simulation being higher than for the experimental chamber and, also, the window sill obstruction to solar exposure is not taken into consideration in this simulation.

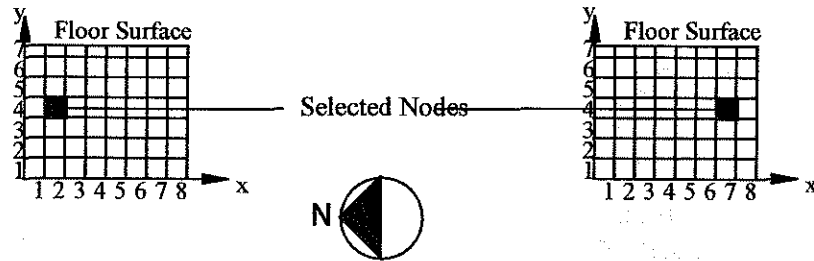
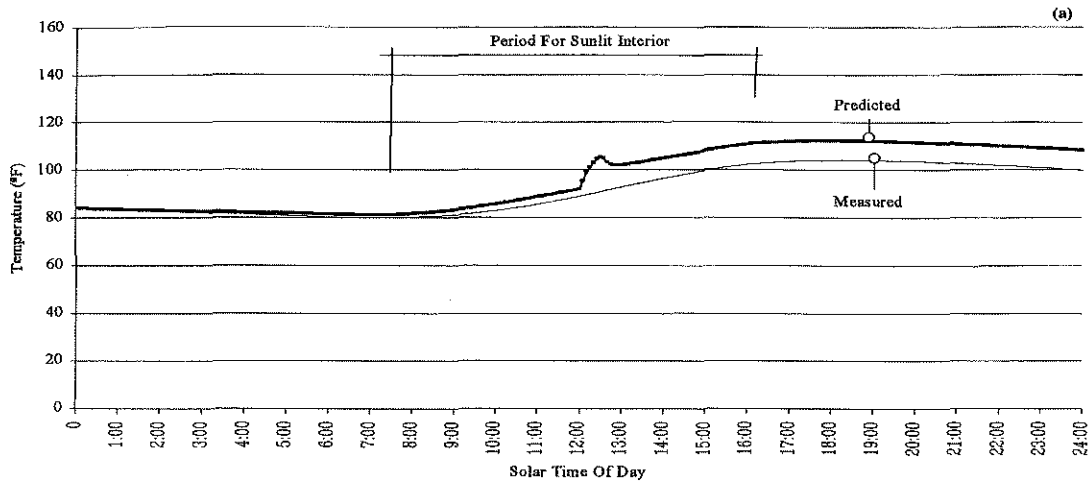
FINDINGS

Examining the maximum temperatures attained by the various interior surfaces, those of the floor and the east wall are the highest, exceeding the rest by up to 20°F. This is largely due to the direct solar radiation striking the floor and east southern nodes at a time when the indoor temperature of air and surface temperatures in general have already increased considerably due to the heat buildup inside the chamber. As more solar heat continues to arrive during the afternoon, the floor and the east wall interior surface temperatures keep rising. By observing the various plots for each surface, the typical range for all other surface temperatures swung from 80°F to 123°F, but for the floor southern part the range is larger, reaching a maximum of 132°F.

This computer simulation indicates that there are quite serious temperature variations occurring along the internal surfaces. On average, differences of 25°F could be observed between exposed and non exposed interior surfaces, according to many other generated plots. In addition, temperature variations occur even between adjacent surfaces, such as between the east and the floor surfaces, with differences also reaching an average of 10°F to 15°F.

The study of these temperature variations would not have been complete without considering the influence they had on the indoor air temperature because of the dynamic solar pattern along the interior surfaces. The temperature of the chamber was allowed to float in response to the outdoor climatic conditions. The prototype space was simplified as

Comparison Between Predicted Versus Measured Temperature For Node 2,4 of Floor Internal Surface



Comparison Between Predicted Versus Measured Temperature For Node 7,4 of Floor Internal Surface

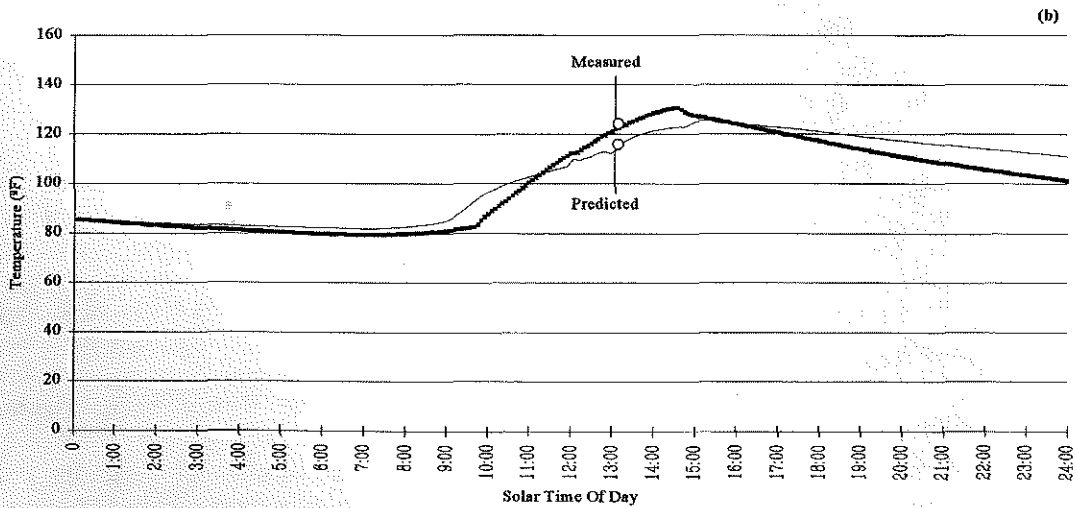


Figure 10 East wall interior surface select nodes, comparison between predicted vs. measured temperatures.

Thermal Performance of Thermal Test Chamber With 2" Reinforced Concrete Mass Layed Over The Entire Internal Floor Surface Area

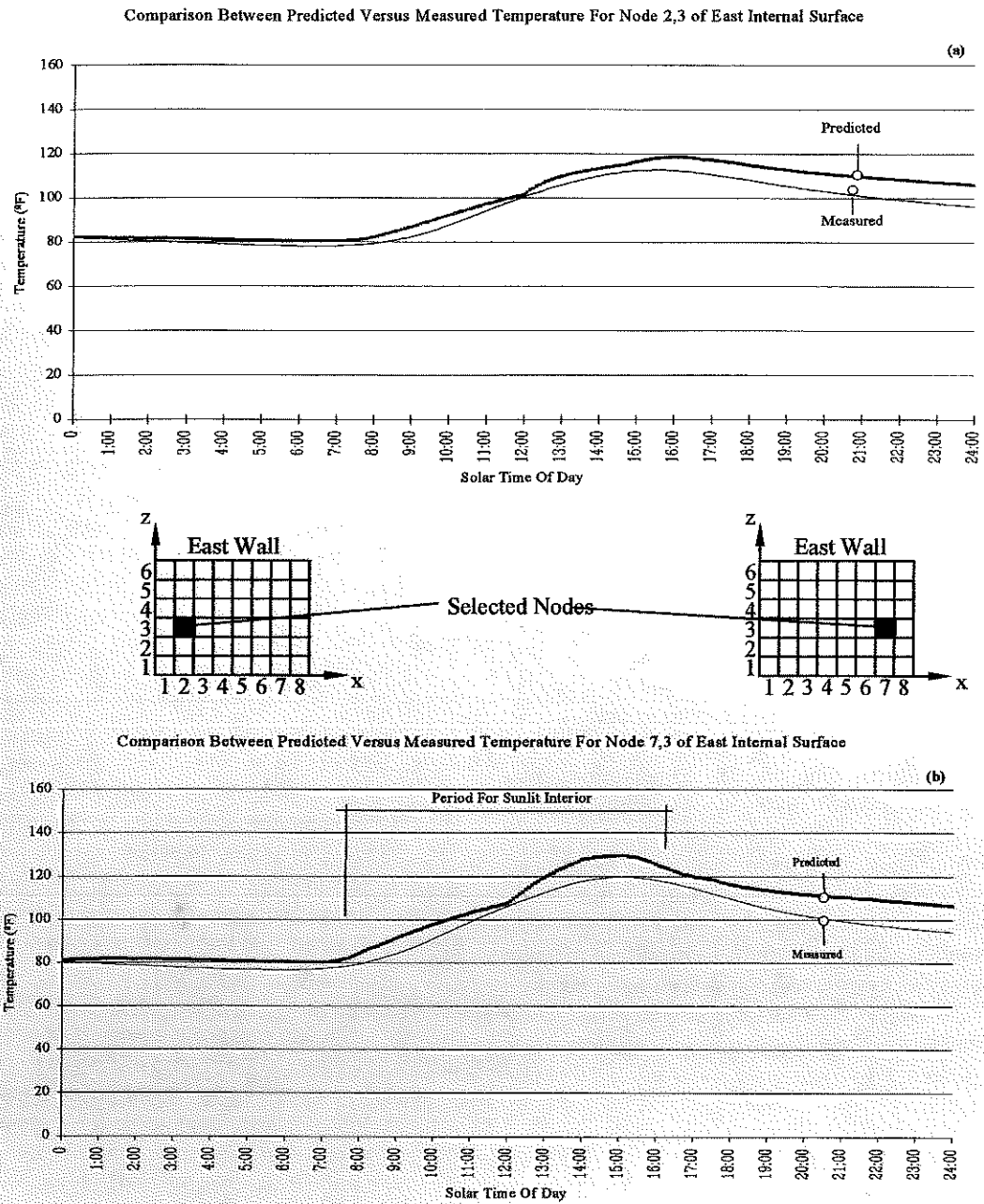


Figure 11. East wall interior surface select nodes, comparison between predicted vs. measured temperatures.

much as possible. Hence, the south window was built out of a single glass pane and purposely was left unshaded. Consequently, the window allowed an excessive amount of heat into the space in comparison to what would have been tolerated in an inhabited environment.

The simulation confirmed, as would be expected, that any interior surface exposed to direct solar radiation shows temperature differences between the lighted and non lighted portions. These variations can be quite extreme, as shown in the simulation. The region of the floor near the window received a large amount of direct insolation. That caused an extreme temperature difference of 22°F (Figure 10) and even up to 27°F in other simulated days between the shaded and unshaded regions of the interior floor surface. This variation in temperature, between the exposed and non exposed areas of the floor, is large enough to demand serious consideration with respect to the design implications of thermal mass use as a heat sink. Thus, the general assumption that the interior room surfaces have uniform temperature seems to overlook a major effect of the solar dynamics.

Location of thermal mass in the insulated region of the west interior surface may not be thermally effective as a heat sink due to the low morning outdoor temperature and solar radiation intensity. The floor, however, which was exposed to higher intensities of solar radiation, has shown a dramatic temperature change from exposed to unexposed area. The large change is the result of the high solar altitude angle at this particular time of the year and, consequently, more nearly perpendicular incidence on the floor, leading to a much higher intake of heat by the exposed region. The temperature of such a region reached an excessive value even with thermal mass on the floor.

Another significant observation needs to be mentioned regarding the temperatures of indoor surfaces. All gridcells that are continuously non exposed, irrespective of the surface, have similar sinuous temporal patterns and similar excursion amplitudes. As soon as the direct solar radiation impinges on some gridcells, they begin to exhibit altered temperature patterns that are more exponential in form and their respective temperatures increase to higher levels than for the non exposed grid units.

LIMITATIONS OF THE COMPUTER MODEL

Although the results obtained with the simulation are in acceptable agreement with the experimental work, there is still need to eliminate some residual discrepancies. First, the morning sunlit surface temperature tends to rise faster and higher than that measured. Second, the performance of the computer simulation showed the predicted temperatures initially started above, then progressed below, the measured temperatures. It is quite difficult to pinpoint a specific reason except to recognize that, by adopting the one-dimensional heat flow assumption, the impact of heat flowing laterally along the surfaces was not included, likely leading to the slight overestimation of

heating effects. Furthermore, the simulation was operated under the assumption of uniform inside air volume temperatures. The present simulation does not include a procedure to deal with nonuniform inside air temperature.

It must also be noted that the reflectivity coefficient of the particle board, and mass interior surface, were not verified independently. In addition, the values of some thermophysical properties for various enclosure components need further verification. Likewise, the empirical use of the convective heat transfer coefficient may have contributed to raising or lowering the predicted temperatures. The simulation does not yet account for the obstruction cast by the window sill at the top of the south knee wall.

CONCLUSION/FURTHER RESEARCH

Balcomb (1982) has published numerous procedures applied to the design of direct gain systems, among them the solar load ratio, the ratio of solar load to building heat load. This method, based on correlations, gives estimates of the lumped thermal mass contribution to the reduction of the average annual heating energy consumption. However, this approach does not provide a detailed evaluation of internal mass placement and its effect on the resulting indoor air temperature. Other studies (Alford et al. 1939; Stephenson and Mitalas 1967; Winslow et al. 1945; Stephenson and Mitalas 1967; Winkelmann 1988) have either focused more on the behavior of a discrete component enclosing the space or on the application of thermal mass to a conditioned space. In the latter, the focus is on the lumped capacitance of mass rather than on its distribution when coupled to direct solar gain. The known simulation programs such as BLAST (CERL 1981), TRANSYS (UW 1988), and DOE-2 (LBL 1982) do not take into consideration the mass layout inside the space; instead, the solar heat is stipulated to be evenly distributed inside a space with a light, medium, or heavy structure.

The summary of temperature equations indicates the transformations made to the initial ASHRAE Handbook heat balance method in order to achieve proper coupling of diffuse and direct solar gain to thermal mass. These modifications were of a geometric order, mainly related to the view factor calculations and the internal insolation computations. After a number of test runs with various time steps, the known stability of the finite difference method, implicit technique, facilitated the selection of a longer time step. The choice of the five-minute time step seemed the most adequate given (1) the time it takes to run this large computer program, (2) the number of iterations performed toward convergence, and (3) the minimal variations observed between one-, two-, three-, four-, and five-minute time steps.

In summary, this work started with an experimental investigation of thermal distribution inside the test chamber. The differences observed between the various interior surface temperatures called for a better modeling of how these surfaces heat or cool through time. Consequently, the model discussed above was developed for the specific physical setup

already described and cannot be generalized to other room geometric configurations. The view factors applied here are for perpendicular and parallel surfaces. The dynamics of the sunlit configurations have been determined for the specific geometry of the test chamber and its south-facing window location. Finally, further work must be undertaken to incorporate the modeling of a space with more than one window.

REFERENCES

- Alford, J.S., J.E. Ryan, and F.O. Urban. 1939. Effect of heat storage and variation in outdoor temperature and solar intensity on heat transfer through walls. *ASHVE Transactions*, Vol. 45, p 369.
- APRL (Architecture and Planning Research Laboratory). 1988. ARCH: LIBRARY programmer's manual. College of Architecture and Urban Planning, University of Michigan.
- ASHRAE. 1989. *1989 ASHRAE Handbook—Fundamentals*, chapter 28. Atlanta: American Society of Heating, Refrigerating and Air-Conditioning Engineers, Inc.
- Balcomb, D.J. 1982. *Passive solar design handbook*, Vol. 2 and 3. New York: American Solar Energy Society, Inc.
- CERL. 1981. *BLAST, Building load analysis simulation and systems thermodynamics user's manual*, Version 3.0. Construction Engineering Research Laboratory.
- Clark, A.J. 1987. Principles of heat transfer. Course ME 475, Mechanical Engineering Department, University of Michigan, Fall 1987.
- Hottel, W.H.C. 1930. Radiant heat transmission. *Journal of Mechanical Engineering*, No. 52, pp. 699-704.
- Incropera, F.P., and D.P. DeWitt. 1985. *Introduction to heat transfer*. New York: John Wiley and Sons, Inc.
- Kusuda, T. 1976. Numerical building simulation. *NBSLD: The computer program for heating and cooling loads in Buildings*. U.S. National Bureau of Standards, Building Science Series 69.
- LBL. 1982. *Department of Energy Engineers' Manual*, DOE-2 Version 2.1A, p. III.71. Berkeley, Calif.: Lawrence Berkeley Laboratory.
- Messadi, T. 1990a. A theoretical procedure to determine configurations of sunlit room surfaces. *ASHRAE Transactions*, pp.39-52.
- Messadi, T. 1990b. Experimental validation of the procedure to determine sunlit configurations on internal room surfaces. *15th National Passive Solar Proceedings, Boulder, Colorado*, Vol. 15, pp.251-256.
- Olsson, C.H. 1989. Interactive computer modeling of energy use in building design, pp. 108-117. Doctoral dissertation, Department of Urban Planning, Lund Institute of Technology, Lund, Sweden.
- Stephenson, D.G., and G.P. Mitalas. 1967. Room thermal response factors. *ASHRAE Transactions*, Vol. 73, pp. III.1.1-III.1.7.
- Stephenson, D.G., and G.P. Mitalas. 1967. Cooling load calculations by thermal response factor. *ASHVE Transactions*, Vol. 73.
- UW. 1988. *TRNSYS, Transient system simulation program manual, version 13.1*. University of Wisconsin-Madison.
- Welty, J.R. 1978. *Engineering heat transfer*. New York: John Wiley and Sons.
- Winkelmann, F. 1988. Advances in building energy simulation in North America. *Energy and Buildings*, No. 10, pp. 161-173.
- Winslow, C.E., L.P. Herrington, and R.J. Lorenzi. 1945. The influence of heat capacity of walls on internal thermal conditions and heat economy. *ASHVE Transactions*, Vol. 51, p. 197.